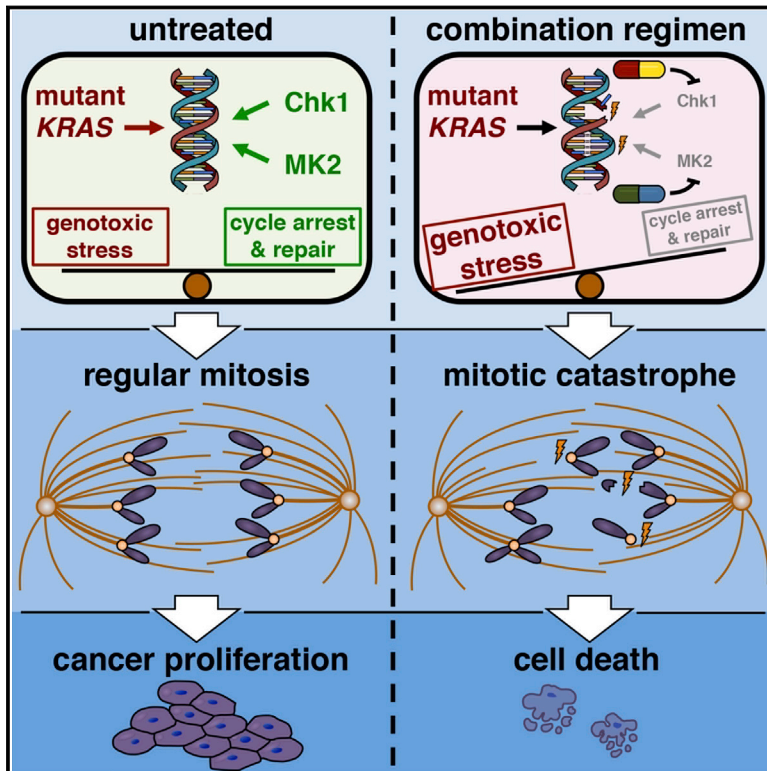# Cell

A Synergistic Interaction between Chk1- and MK2 Inhibitors in *KRAS*-Mutant Cancer

Graphical Abstract

Authors

Felix Dietlein, Bastian Kalb,
Mladen Jokic, ..., Reinhard Büttner,
Roman K. Thomas, H. Christian Reinhardt

Correspondence

fdietlei@smail.uni-koeln.de (F.D.),
christian.reinhardt@uk-koeln.de (H.C.R.)

In Brief

PreCISE, a new platform that reliably captures synergic drug interactions from large-scale cell-line-based screens, shows that simultaneous inhibition of the cell-cycle checkpoint kinases Chk1 and MK2 effectively eradicates KRAS-mutant cancer cells directly isolated from patients and in distinct Kras-driven murine tumor models.

Highlights

- The PreCISE software accurately captures synergistic drug interactions

- Combined Chk1/MK2 inhibition synergistically induces apoptosis in *KRAS*-mutant cancer

- *KRAS*-mutant tumor cells display a tonic activation of the DNA damage response

- Autochthonous *Kras*-driven tumors display non-oncogene addiction to Chk1 and MK2

CrossMark

CellPress

A Synergistic Interaction between Chk1- and MK2 Inhibitors in *KRAS*-Mutant Cancer

Felix Dietlein,[1,2,*] Bastian Kalb,[1,2] Mladen Jokic,[1,2] Elisa M. Noll,[3,4] Alexander Strong,[5] Lars Tharun,[6] Luka Ozretić,[6] Helen Künstlinger,[6] Kato Kambartel,[7,8] Winfried J. Randerath,[7,9] Christian Jüngst,[2] Anna Schmitt,[1,2] Alessandro Torgovnick,[1,2] André Richters,[10] Daniel Rauh,[10] Florian Siedek,[11] Thorsten Persigehl,[11] Cornelia Mauch,[12] Jirina Bartkova,[13,14,15] Allan Bradley,[5] Martin R. Sprick,[4] Andreas Trumpp,[3,4,16] Roland Rad,[17] Dieter Saur,[17] Jiri Bartek,[13,14,15] Jürgen Wolf,[1,7] Reinhard Büttner,[6,7] Roman K. Thomas,[6,18] and H. Christian Reinhardt[1,2,*]

[1]Department I of Internal Medicine, University Hospital Cologne, Weyertal 115B, 50931 Cologne, Germany
[2]CECAD, University of Cologne, Weyertal 115B, 50931 Cologne, Germany
[3]Division of Stem Cells and Cancer, Deutsches Krebsforschungszentrum, Im Neuenheimer Feld 280, 69120 Heidelberg, Germany
[4]Heidelberg Institute for Stem Cell Technology and Experimental Medicine, Im Neuenheimer Feld 280, 69120 Heidelberg, Germany
[5]The Wellcome Trust Sanger Institute, Genome Campus, Hinxton, Cambridge CB10 1SA, UK
[6]Institute of Pathology, University Hospital Cologne, Kerpener Strasse 62, 50937 Cologne, Germany
[7]Network Genomic Medicine, University Hospital Cologne, Kerpener Strasse 62, 50937 Cologne, Germany
[8]Lungenklinik, Krankenhaus Bethanien Moers, Bethanienstraße 21, 47441 Moers, Germany
[9]Klinik für Pneumologie, Krankenhaus Bethanien Solingen, Aufderhöher Strasse 169-175, 42699 Solingen, Germany
[10]Department of Chemistry and Chemical Biology, Technische Universität Dortmund, Otto-Hahn-Strasse 6, 44227 Dortmund, Germany
[11]Department of Radiology, University Hospital Cologne, Kerpener Strasse 62, 50937 Cologne, Germany
[12]Department of Dermatology, University Hospital Cologne, Kerpener Strasse 62, 50937 Cologne, Germany
[13]Danish Cancer Society Research Center, Strandboulevarden 49, 2100 Copenhagen, Denmark
[14]Institute of Molecular and Translational Medicine, Palacky University, Hněvotínská 1333/5, 77900 Olomouc, Czech Republic
[15]Science for Life Laboratory, Division of Translational Medicine and Chemical Biology, Department of Medical Biochemistry and Biophysics, Karolinska Institute, 17177 Stockholm, Sweden
[16]German Cancer Consortium, Im Neuenheimer Feld 280, 69120 Heidelberg, Germany
[17]Department of Internal Medicine II, Klinikum rechts der Isar, Technische Universität München, Ismaninger Strasse 22, 81675 München, Germany
[18]Department of Translational Genomics, Medical Faculty, University of Cologne, Weyertal 115B, 50931 Cologne, Germany
*Correspondence: fdietlei@smail.uni-koeln.de (F.D.), christian.reinhardt@uk-koeln.de (H.C.R.)
http://dx.doi.org/10.1016/j.cell.2015.05.053

SUMMARY

KRAS is one of the most frequently mutated onco-genes in human cancer. Despite substantial efforts, no clinically applicable strategy has yet been developed to effectively treat *KRAS*-mutant tumors. Here, we perform a cell-line-based screen and identify strong synergistic interactions between cell-cycle checkpoint-abrogating Chk1- and MK2 inhibitors, specifically in *KRAS*- and *BRAF*-driven cells. Mechanistically, we show that *KRAS*-mutant cancer displays intrinsic genotoxic stress, leading to tonic Chk1- and MK2 activity. We demonstrate that simultaneous Chk1- and MK2 inhibition leads to mitotic catastrophe in *KRAS*-mutant cells. This actionable synergistic interaction is validated using xenograft models, as well as distinct *Kras*- or *Braf*-driven autochthonous murine cancer models. Lastly, we show that combined checkpoint inhibition induces apoptotic cell death in *KRAS*- or *BRAF*-mutant tumor cells directly isolated from patients. These results strongly recommend simultaneous Chk1- and MK2 inhibition as a therapeutic strategy for the treatment of *KRAS*- or *BRAF*-driven cancers.

INTRODUCTION

In response to genotoxic stress, cells activate a complex, kinase-based signaling network, which is commonly referred to as the DNA damage response (DDR) (Jackson and Bartek, 2009). Cells progress through a series of cell-cycle checkpoints prior to mitosis. These checkpoints allow time to repair DNA lesions or, if damage is excessive, lead to the induction of apoptosis (Jackson and Bartek, 2009). Thus, checkpoint signaling can be seen as an effective fail-safe mechanism to provide and maintain genome stability through cell-cycle arrest with subsequent DNA repair or apoptotic elimination of mutated, incipient cancer cells.

The canonical DDR network consists of two major kinase signaling branches, which operate through the upstream kinases ATR and ATM, as well as their downstream effector kinases Chk1 and Chk2, respectively (Jackson and Bartek, 2009). A third checkpoint effector pathway, mediated through TAO- and p38-dependent MK2 activity, was recently identified (Reinhardt and Yaffe, 2013). The p38/MK2 pathway is a global stress-kinase pathway that operates in parallel to Chk1. In response to DNA damage, this pathway is recruited as part of the ATM/ATR-dependent checkpoint signaling network (Reinhardt and Yaffe, 2013). Chk1 and MK2 control checkpoint initiation and maintenance, respectively (Reinhardt et al., 2010). The activity of both kinases converges on mediating inhibitory phosphorylations on

CDC25 family members to induce a subsequent cell-cycle arrest by blocking CDC25B-dependent CDK activation (Reinhardt and Yaffe, 2013).

We predicted that simultaneous Chk1- and MK2 inhibition might result in synergistic effects through efficient checkpoint abrogation. In spite of the clinical need for targeted combination therapies, no generally accepted experimental and mathematical procedures for the reliable detection of synergistic drug interactions have been implemented thus far. For this purpose, we developed a software tool that was specifically engineered to enable a reliable detection of synergistic drug interactions and allows integration with genomic data. Using this tool, we addressed the question of whether inhibition of Chk1 and MK2 results in synergistic cytotoxic effects. Surprisingly, we found that *KRAS*-mutant cell lines display an actionable dependence on functional checkpoint signaling. These observations were validated in murine models and primary patient material.

RESULTS

Development of a Computational Tool to Identify Synergistic Drug Interactions

The biological effect of a given compound is typically measured by its GI_{50} value, which defines the concentration at which the half-maximal biological effect is observed (Dietlein et al., 2014). For this purpose, biological effects are usually determined at various concentrations (Supplemental Experimental Procedures, General Outline, Notation and Definitions, and Interpolation of Compound Activity sections). Based on their single-agent activities, the combined effect of two compounds can be classified as additive, synergistic, or antagonistic. To detect synergistic interactions, an appropriate model for compound additivity and a measure of synergistic deviation from this model are required.

We developed a potency-adapted compound additivity model (PACAM), which generalizes the concept of Loewe additivity (Loewe, 1953) to non-linear dose-effect relationships (Supplemental Experimental Procedures, Additivity Models section). PACAM generates a GI_{50} curve that runs through all concentration pairs for which single-agent activities add up to half-maximal effect (Figure S1A). We compared the PACAM-derived GI_{50} curve with an experimentally observed GI_{50} curve and quantified the area enclosed by these curves (synergy area) as a measure for synergy. Depending on the relationship between expected and observed GI_{50} curves, additive, synergistic, and antagonistic drug interactions can be discriminated (Supplemental Experimental Procedures, Synergism Quantification section).

To facilitate automated synergism calculations in high-throughput screens, we developed the PreCISE (predictor of chemical inhibitor synergistic effects) software (Data S1). PreCISE derives synergism scores from two-dimensional matrices consisting of cytotoxicity data achieved by combinations of two compounds applied at individually varying concentrations. In essence, a matrix consisting of $m \times n$ individual cytotoxicity measurements is derived from m concentrations of compound *A* combined with n concentrations of compound *B* (Figure 1A, top left). For each cell line examined, PreCISE first generates an expected GI_{50} curve derived from single-agent activity

(Figure 1A, bottom left) based on our PACAM model (Figure 1A, bottom middle; Supplemental Experimental Procedures, Additivity Models section). Next, PreCISE derives an observed GI_{50} curve from experimental data (Figure 1A, top middle, Supplemental Experimental Procedures, Interpolation of Compound Activity section). The synergy area enclosed by the observed and expected GI_{50} curves is then quantified by PreCISE (Figure 1A, top right, orange area; Supplemental Experimental Procedures, Synergism Quantification section). This allows discrimination between additive, synergistic, or antagonistic interactions (Figure 1A, bottom right). Further, PreCISE inspects the concentration matrix to determine the optimal dose combination at which maximal synergy is achieved (Figure 1A, bottom right; Supplemental Experimental Procedures, Synergism Quantification section). Finally, PreCISE derives a measure for the quality of the screening data, which then allows the automated identification of those cell lines for which screening data are too noisy to allow a definite interpretation (Supplemental Experimental Procedures, Synergism Quantification section).

We tested PreCISE against previously published approaches for synergy calculation. Compared with synergism scores derived by Bliss independence, we found that PreCISE displayed improved compensation of technical data noise (Figure S1B). Further, PreCISE was in strong concordance with the Horizon Chalice Analyzer Software (Figure S1C), which quantifies synergy based on an elevated Loewe model (Lehár et al., 2009). This confirmed the general validity of our approach.

A Cell-Line-Based Screen Identifies Oncogenic *KRAS* as a Predictor for Synergistic Interactions between Chk1- and MK2 Inhibitors

Single-agent checkpoint abrogators have largely failed to show clinical efficacy (Curtin, 2012). We hypothesized that combined checkpoint inhibition through the use of Chk1- and MK2 inhibitors might overcome this limitation, as these kinases operate in parallel pathways (Reinhardt et al., 2010). In order to identify synergistic interactions between Chk1- and MK2 inhibitors on a panel of 96 cancer cell lines, we employed PreCISE to analyze combinatorial cytotoxic effects of both compounds at six varying concentrations (Figure 1B and Table S1). We used PF477736 and PF3644022 as specific Chk1- and MK2 inhibitors, respectively.

We observed strong synergistic effects between PF477736 and PF3644022 in 33 out of the 96 cell lines (referred to as synergistic lines) (Figure 1B, Table S1, and Data S2). These effects appeared to be specific to dual checkpoint abrogation, as replacement of the Chk1 inhibitor PF477736 with the PARP1 inhibitor AZD2281 did not display any synergy with the MK2 inhibitor (Figure 1B).

We next aimed to identify recurrent genetic alterations that dictate the synergistic effects between Chk1- and MK2 inhibitors. To this end, we compared the mutation frequency of 1,319 cancer-associated genes between synergistic and non-synergistic cell lines (Supplemental Experimental Procedures, Selection of Mutations and Significance of Mutations as Synergy Predictors sections). As a further measure of predictive strength, we calculated the ratio of synergy scores between mutant and non-mutant cell lines (synergy ratio) (Figure 1C and
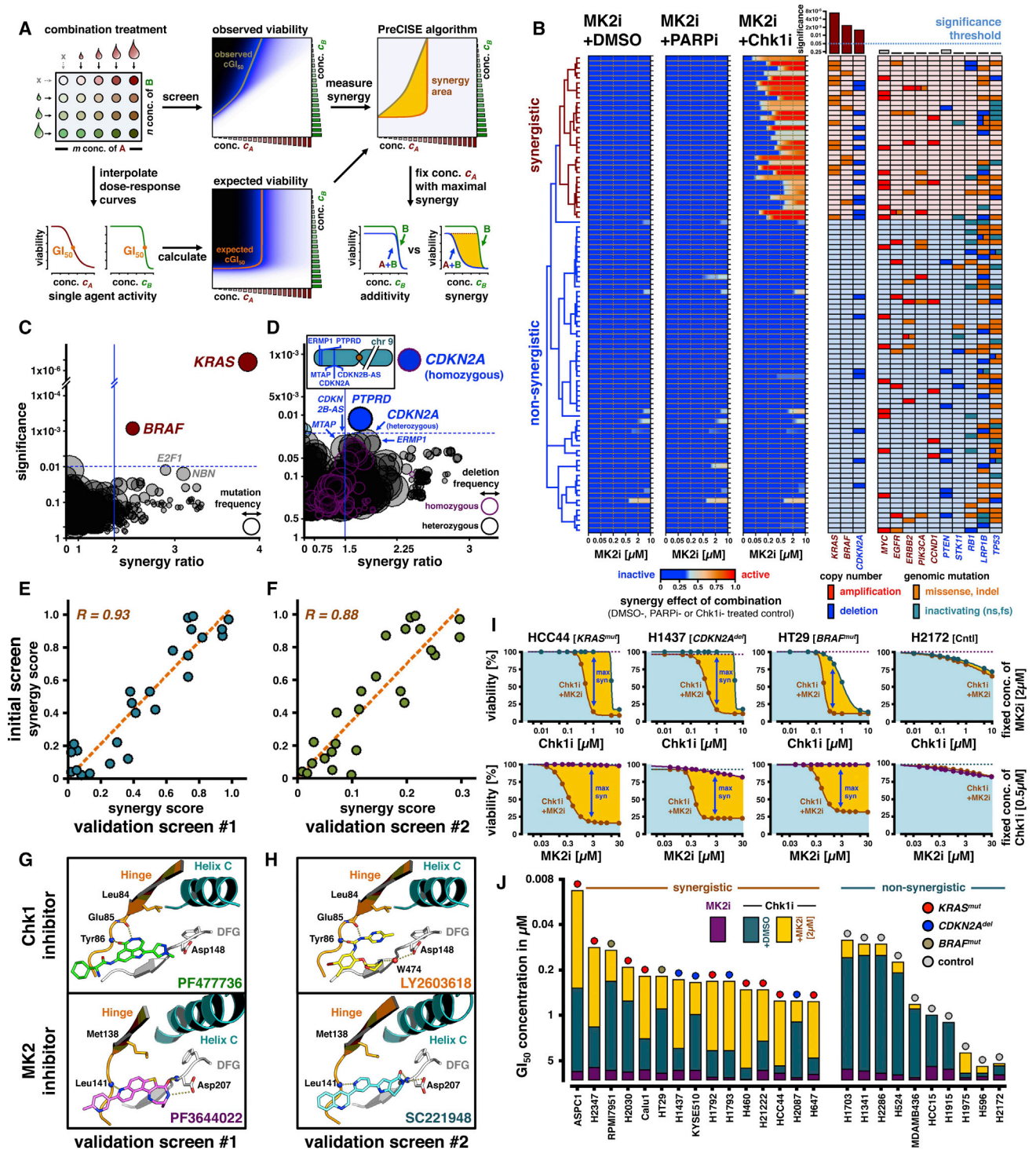
Figure 1. A Compound Interaction Screen Reveals a Synergistic Interaction between Chk1- and MK2 Inhibitors in *KRAS*-Mutant Cancer

(A) Scheme of the PreCISE algorithm for the detection of synergistic interactions between compounds A (red) and B (green). Viability measurements in response to $m \times n$ concentration (conc.) pairs (top left) were used to derive single-agent activities (bottom left) and an observed cGI_{50} curve (brown, top middle). Based on the activity of A and B, an expected cGI_{50} curve (orange) was inferred (bottom middle). The synergy area (orange) enclosed by the observed and expected curves (top right) served as a measure for synergy between A and B. PreCISE returns either additive or synergistic effects between compounds A and B (bottom right). See Figures S1A–S1C for further technical details about PreCISE. See Data S1 for an executable version of the PreCISE software.

(legend continued on next page)

Supplemental Experimental Procedures, Synergy Ratios section). In brief, we separated the screening panel into mutant and wild-type cells for each gene. We then determined the average synergy for both of these sub-cohorts and then calculated the ratio between these values. We found that oncogenic *KRAS* mutations emerged as the most significant (q = 5.68 × 10^{-7}) mutational predictor for synergistic effects between Chk1- and MK2 inhibitors (Figure 1C). Furthermore, *KRAS* displayed the highest synergy ratio of all the 1,319 genes (R = 3.89). Although substantially less significant, activating mutations in *BRAF* (q = 1.19 × 10^{-3}), which is a direct downstream target of KRAS, emerged as an additional predictor of synergy between Chk1- and MK2 inhibitors (Figure 1C).

We next validated the specificity of *KRAS* and *BRAF* mutations as predictors of synergism between Chk1- and MK2 inhibitors in isogenic NIH3T3 cell lines that were transduced with an empty vector, *EGFR*[L858R], *KRAS*[G12V], or *BRAF*[V600E] (Figures S1D and S1E). As shown in Figure S1D, combined inhibition of Chk1 and MK2 induced massive apoptosis specifically in *KRAS*[G12V]- and *BRAF*[V600E]-expressing cells, whereas neither compound alone resulted in substantial apoptosis. We next assessed the long-term effect of dual checkpoint inhibition using clonogenic survival assays. These experiments revealed an almost complete eradication of *KRAS*[G12V]- and *BRAF*[V600E]-expressing cells, whereas empty vector- or *EGFR*[L858R]-transduced cells were unaffected following 72 hr of simultaneous Chk1/MK2 inhibition. Single-agent Chk1 or MK2 inhibition had no substantial effect in any of these assays (Figure S1E).

We next examined whether recurrent focal somatic copy number alterations (SCNAs) might predict synergistic effects between Chk1- and MK2 inhibitors. For this purpose, we compared synergistic and non-synergistic cell lines at each genomic locus, which displayed recurrent focal SCNAs (Supplemental Experimental Procedures, Copy Number Analysis section). As shown in Figure 1D, focal and homozygous deletions of *CDKN2A* were significantly enriched (q = 1.42 × 10^{-3}) in the cohort of synergistic cell lines and constituted the most significant SCNA-based predictor for synergy between Chk1- and MK2 inhibitors. Several genes located in close genomic proximity to *CDKN2A*, such as *PTPRD*, also emerged as significant predictors (Figure 1D). However, RNAi-mediated *Cdkn2a* depletion in NIH 3T3 cells rendered these cells sensitive against combined Chk1 and MK2 inhibition, both in apoptosis and colony survival assays (Figures S1D and S1E).

Together, our data suggest that activating *KRAS* or *BRAF* mutations and *CDKN2A* deletions are associated with non-oncogene addiction to checkpoint signaling (Figures 1C, 1D, S1D, and S1E), as evidenced by a synergistic drug interaction between Chk1- and MK2 inhibitors (Figure 1B). Other potent cancer-driving genomic aberrations, such as mutations in *EGFR*, *PIK3CA*, and *LRP1B*, as well as amplifications of *MYC* and *ERBB2* or deletions of *PTEN*, although well-represented in our cell line panel, did not significantly co-cluster with sensitivity to dual checkpoint blockade (Figure 1B).

Pharmacological and Genetic Validation of the Synergistic Interaction between Chk1- and MK2 Inhibitors

To validate the reproducibility of our screening data, we compiled a 25 cell line re-examination panel consisting of nine *KRAS*-mutant lines (HCC44, H2030, H1792, H2347, H460, H647, H2122, ASPC1, and Calu1), two *BRAF*-mutant lines (RPMI7951 and HT29), four *CDKN2A*-deleted lines (H1437, H1793, H2087, and KYSE510), and ten non-synergistic control lines (H1341, H1703, H524, H2286, H596, H2172, H1975, H1915, HCC15, and MDAMB436). We re-profiled this panel using a matrix consisting of 10 × 12 concentration pairs (validation screen 1, Figure 1E). To exclude structure-specific off-target effects, we re-screened the re-examination panel by replacing PF477736 and PF3644022 with alternative Chk1- and MK2

(B) Synergy screening of 96 cell lines reveals a synergistic interaction between Chk1- and MK2 inhibitors. Cells were treated with 6 × 6 concentration pairs of PF3644022 (MK2i) in combination with either AZD2281 (PARPi) or PF477736 (Chk1i). Heatmaps encode synergistic effects induced by PF3644022 on cell lines that were either exposed to DMSO (left), AZD2281 (2 μM), or PF477736 (0.5 μM). Cell lines were arranged into synergistic (red) and non-synergistic cell lines by hierarchical clustering of expression signatures (clustering tree). Mutation and SCNA status of 13 genes are annotated. Gene alteration frequencies are compared between synergistic and non-synergistic cell lines (false-discovery rates, top). See Table S1 for annotation and screening results. See Data S2 for the raw data of this screen.

(C and D) Volcano plot representation of a systematic association of mutations (C) and deletions (D) in 1,319 genes with synergistic interaction between Chk1- and MK2 inhibitors. For each gene, significance (false discovery rate, y axis) is plotted against the ratio of average synergism scores in mutant/deleted versus non-mutant/non-deleted cell lines. Genes for which mutation (C) or deletion (D) status are significantly associated with synergistic compound interaction are colored in red or blue, respectively. Circle sizes encode mutation (C) or deletion (D) frequency. (D) Inset: genomic position of significant genes on chromosome 9. See Figures S1D and S1E for a validation of the specificity of mutations and deletions.

(E and F) The synergistic interaction between PF477736 and PF3644022 (validation screen 1, [E]) as well as LY2603618 and SC221948 (validation screen 2, [F]) was examined across a panel of 25 cell lines and correlated (Pearson correlation, *R*) with the synergy scores obtained in the in the initial screen. Orange dashed lines depict least-squares regression. See Figures S2A and S2B for a genetic validation of compound targets by RNAi.

(G and H) Illustration of inhibitor binding by ribbon diagrams (turquoise, helix C; orange, hinge region; gray, DFG motif; blue sphere, peptide backbone NH; red sphere, water molecule; yellow dots, hydrogen bonds). Anticipated binding modes of PF477736 ([G], top) and LY2603618 ([H], top) were modeled into the Chk1 ATP binding cleft (PDB: 4FT5) based on either a pharmacophore model or the crystal structure of a closely related homolog (PDB: 4FT5). The binding mode of PF3644022 ([G], bottom) into the MK2 ATP binding pocket was derived from the appropriate complex crystal structure (PDB: 3FYJ). SC221948 ([H], bottom) was fit into the MK2 ATP binding cleft by adapting the conformation of a closely related analog (PDB: 2P3G).

(I) Identification of inhibitor concentration pairs, which result in maximal synergistic effects. Concentration optimization is shown for three synergistic cell lines (HCC44, H1437, and HT29) and one non-synergistic control (H2172). Dose-response curves (logistic interpolation) of PF477736 (Chk1i) in the presence (brown) or absence (turquoise) of a fixed concentration of PF3644022 (2 μM, MK2i) were compared (top). Vice versa, activity of PF3644022 was compared in the absence or presence of a fixed concentration (0.5 μM) of PF477736 (bottom). Blue arrows mark inhibitor concentrations, which display maximal synergistic effects.

(J) MK2 inhibition sensitizes synergistic cells to Chk1 inhibition. The stacked bar graph displays the half maximal inhibitory concentrations (GI_{50}) of PF3644022 (purple, MK2i) and PF477736 (Chk1i) in the absence (turquoise) or presence (orange) of PF3644022 (2 μM, MK2i) across 25 cell lines.

inhibitors that were based on entirely distinct chemical motifs (Figure 1F). PF477736 was exchanged against the pyrazinyl-urea LY2603618, and PF3644022 was replaced with the pyrrolo-pyridinone SC221948 (validation screen 2, Figures 1G and 1H). The synergy scores retrieved in both re-screening experiments were highly correlated with the results from our initial screen (R = 0.93, validation screen 1; R = 0.88, validation screen 2, Figures 1E and 1F).

For target validation, we used RNAi to deplete Chk1 and/or MK2 in three synergistic cell lines and two non-synergistic controls (Figure S2A). Co-transduction with shRNAs targeting Chk1 and MK2 resulted in substantial cytotoxicity with less than 9% survival in the synergistic cell lines, whereas the control lines remained largely unaffected (Figure S2B). Isolated depletion of Chk1 induced a mild reduction of cellular viability, whereas knockdown of MK2 had no substantial effect (Figure S2B). Thus, genetic repression of Chk1 and MK2 phenocopied the effects observed when these kinases were pharmacologically inhibited.

Finally, we aimed to determine the PF477736 and PF3644022 concentrations at which the strongest synergistic interaction could be observed. To this end, we compared the efficacy of each compound in the presence or absence of a stepwise fixed concentration of the second inhibitor (Figure 1I). This analysis revealed that a combination of 0.5 μM PF477736 and 2.0 μM PF3644022 maximized the synergistic effects. Using these concentrations, the potency of PF477736 and PF3644022 as single agents and in combination was quantified on the panel of 25 cell lines that we had used in the validation screens (Figures 1E and 1F). As shown in Figure 1J, MK2 inhibition did not substantially reduce cellular viability when PF3644022 was used at concentrations up to 7.5 μM. Although the Chk1 inhibitor PF477736 led to a moderate viability reduction in the majority of cell lines, when used as a single agent, addition of 2.0 μM PF3644022 dramatically and selectively sensitized the panel of synergistic cell lines to Chk1 inhibition (median 10.3-fold reduction in GI$_{50}$ of PF477736, p = 8.1 $\times$ 10^{-4}). In contrast, addition of the MK2 inhibitor to the non-synergistic lines did not result in any relevant increase in Chk1 inhibitor toxicity (median 1.4-fold GI$_{50}$ reduction). Thus, we applied PF477736 at 0.5 μM and PF3644022 at 2 μM in all subsequent experiments.

Dual Chk1/MK2 Inhibition Induces Apoptosis in *KRAS*-Mutant Cancer Cells
To investigate whether combined Chk1/MK2 inhibition induces apoptosis in synergistic cell lines, we assessed Annexin V/propidium iodide (PI) double-positive cells in our re-examination panel (Figures 2A, 2B, and S2C). Cells were exposed to PF477736 (0.5 μM), PF3644022 (2.0 μM), or a combination regimen for 0, 24, 48, and 72 hr. Combination treatment massively enhanced the apoptosis observed in the synergistic cell lines, compared to the effect of either compound alone. In contrast, addition of the MK2 inhibitor to Chk1 inhibitor-treated non-synergistic cell lines did not enhance the effects induced by PF477736 (Figures 2A, 2B, and S2C).

We next performed clonogenic survival assays. Cultures were exposed to PF477736 (0.5 μM), PF3644022 (2.0 μM), or a combination for 7 days. Inhibition of MK2 alone did not lead to

a substantial reduction in surviving colonies, whereas the Chk1 inhibitor induced a moderate reduction in clonogenic survival in the synergistic cell lines. However, combined inhibition of both Chk1 and MK2 almost completely eradicated the *KRAS*-, *BRAF*-, or *CDKN2A*-altered cell lines, whereas non-synergistic cell lines remained largely unaffected by the combination (Figures 2C, 2D, and S2D).

To further substantiate the synergistic effect of combined Chk1/MK2 inhibition specifically in *KRAS*- or *BRAF*-mutant cell lines, we next analyzed an additional panel of 18 *KRAS*- and 6 *BRAF*-mutant human and murine cell lines that were not included in the initial screening panel (Figures S3A and S3B). Concordant with the data reported in Figures 1 and 2, we observed a significant synergistic interaction between Chk1- and MK2 inhibitors in *KRAS*- (Figures S3C and S3D, p = 4.94 $\times$ 10^{-5}) and *BRAF*-mutant (Figures S3C and S3D, p = 1.15 $\times$ 10^{-3}) cell lines. Of note, these mutations preserved significance, even when the genetic analysis was restricted to the sub-cohorts of pancreatic, lung, and colorectal adenocarcinomas (Figure S3E). In contrast, we found that single-agent activity of the Chk1 inhibitor PF477736 was restricted to a subset of histotypes, including small-cell and squamous cell lung cancer, as well as hematopoetic malignancies (Figure S3F). We conclude that *KRAS*- and *BRAF* mutations are robust predictors of synergistic interactions between Chk1- and MK2 inhibitors.

Dual Checkpoint Blockade Abolishes CDC25B Phosphorylation in *KRAS*-Mutant Cells
To validate the activity of PF477736 and PF3644022, we assessed their impact on the catalytic activity of Chk1 and MK2 by immunoblotting. Chk1 activity was gauged with an antibody against the autophosphorylation site Ser-296, whereas pSer-82 on HSP27 served as a marker for MK2 activity. Addition of PF477736 led to a marked reduction of pSer-296 Chk1 in all six cell lines examined (Figure 2E). Similarly, PF3644022 strongly reduced pSer-82 HSP27 in all lines, except for H1703 cells, in which no basal HSP27 phosphorylation was detectable. Etoposide treatment served as a positive control for Chk1 and MK2 activation (Figure 2E). These experiments demonstrate that biochemical target inhibition is achieved with the doses of PF477736 and PF3644022 used in this study. We note that baseline pChk1 and pHSP27 appeared to be increased in synergistic cells compared to non-synergistic cells (Figure 2E), suggesting that both Chk1 and MK2 are tonically active in untreated synergistic cell lines.

Given the basal activity of Chk1 and MK2 that we observed in the synergistic lines, we speculated that this activity might translate into enhanced basal CDC25B phosphorylation. Thus, we assessed the levels of pSer-323 CDC25B in five synergistic lines, four non-synergistic lines, and the Chk1 inhibitor-sensitive H1703 cells. We observed a significant (p =0.005) baseline hyperphosphorylation of CDC25B in all five synergistic cell lines, whereas none of the non-synergistic cell lines displayed any substantial pCDC25B. H1703 cells displayed pCDC25B levels similar to the synergistic lines (Figures S4A and S4B).

To corroborate the hypothesis that *KRAS*- or *BRAF*-induced DNA damage leads to checkpoint activation and CDC25B inhibition, we employed an isogenic system. NIH3T3 cells were
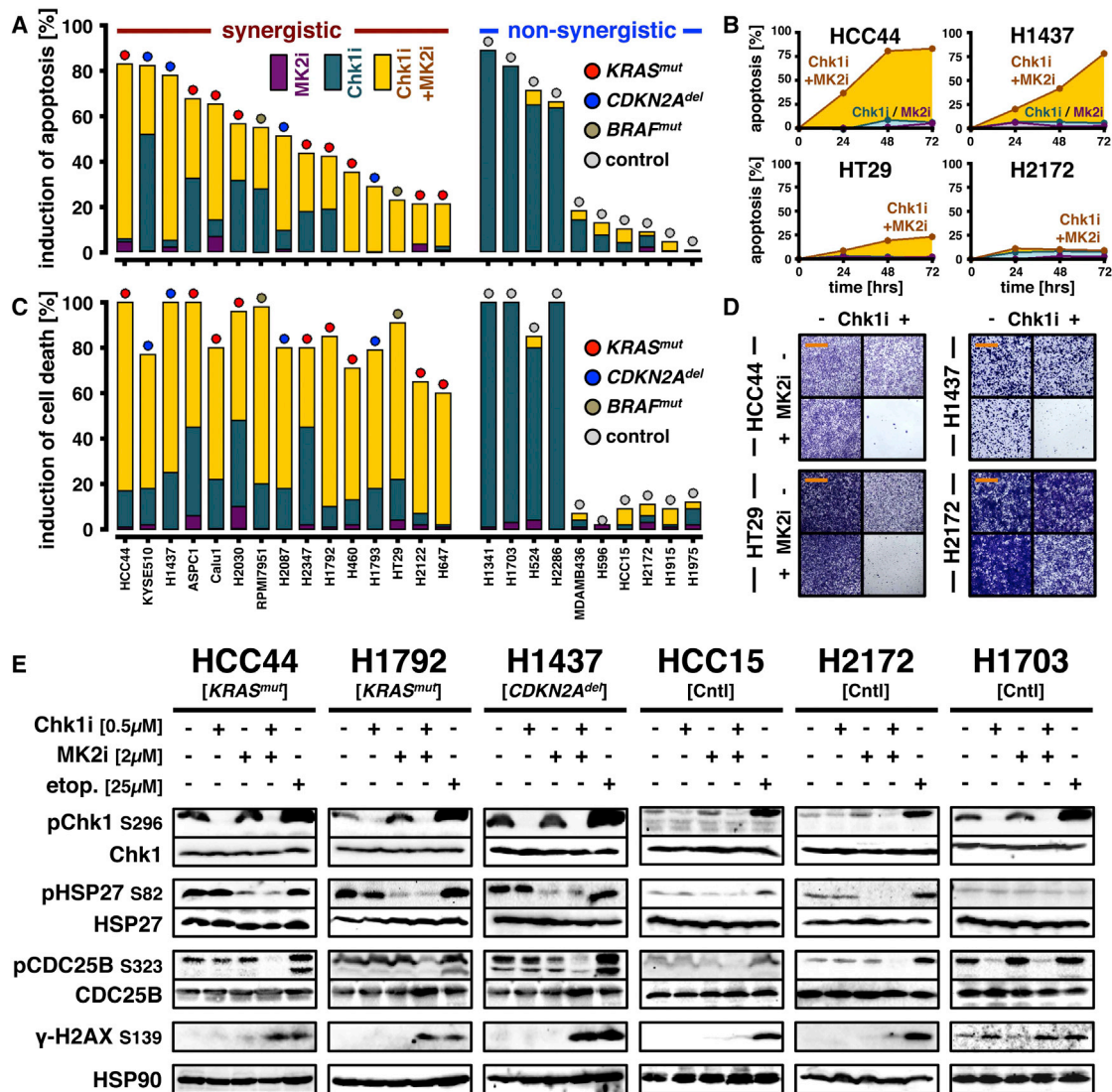
Figure 2. Simultaneous Inhibition of Chk1 and MK2 Induces Genotoxic Stress and Apoptosis in *KRAS*-Driven Cancer Cells

(A) Inhibition of MK2 substantially increases the apoptotic effects induced by the Chk1 inhibitor PF477736 specifically in synergistic cell lines. A panel of 15 synergistic (red) and 10 non-synergistic (blue) cell lines was exposed to PF477736 (0.5 μM), PF3644022 (2 μM), or a combination (Chk1+MK2i) for 72 hr. The stacked bar graph displays the induction of apoptosis, as assessed through flow-cytometry-based measurement of the Annexin V/PI double-positive population.

(B) Measurement of apoptosis (24, 48, and 72 hr) under isolated or combined inhibition of Chk1 and MK2 is shown for three synergistic lines (HCC44, H1437, and HT29) and one non-synergistic control (H2172). See Figure S2C for apoptosis measurements on the residual cell lines.

(C) Inhibition of MK2 increases the cytotoxic effects induced by the Chk1 inhibitor PF477736 specifically in synergistic cell lines. A panel of 25 cell lines was exposed to PF477736 (0.5 μM, Chk1i) and PF3644022 (2 μM, MK2i) alone or in combination (Chk1i+MK2i) for 7 days. The stacked bar graph displays the induction of cell death, which was determined as the relative difference between cell counts of compound- and vehicle-treated cultures.

(D) Clonogenic survival assays under isolated or combined 7 day inhibition of Chk1 (Chk1i) and MK2 (MK2i) are shown for three synergistic lines (HCC44, H1437, and HT29) and one non-synergistic control (H2172). Scale bars, 500 μm. See Figure S2D for assays on eight additional lines. See Figure S3 for a validation of the data shown in Figures 2A–2D on an independent cell line panel.

(E) Combined inhibition of Chk1 and MK2 abrogates CDC25B phosphorylation and induces genotoxic stress in synergistic cell lines. A panel of three synergistic cell lines (HCC44, H1792, and H1437) two non-synergistic controls (HCC15 and H2172), and one Chk1 inhibitor-sensitive cell line (H1703) was exposed to PF477736 (0.5 μM, Chk1i), PF3644022 (2 μM, MK2i), or a combination regimen for 12 hr. A 2 hr pulse of etoposide (25 μM) served as a positive control for induction of DNA damage and checkpoint activation. pSer-296 Chk1, pSer-82 HSP27, and pSer-323 CDC25B were determined by immunoblotting. γ-H2AX served as a marker for genotoxic stress. Total protein levels of Chk1, HSP27, CDC25B, and HSP90 served as controls. See Figures S4A–S4F for basal phosphorylation of CDC25B and H2AX.

transduced with an empty vector, $EGFR^{L858R}$, $KRAS^{G12V}$, $BRAF^{V600E}$, or a $Cdkn2a$ short hairpin RNA (shRNA). We observed a significant (p = 0.039) hyperphosphorylation of CDC25B in $KRAS^{G12V}$-, $BRAF^{V600E}$-, and $Cdkn2a$ shRNA-expressing cells, compared to empty vector and $EGFR^{L858R}$ controls (Figure S4C). We further found robust pCDC25B staining in human pancreatic ductal adenocarcinoma specimens (n = 39), an entity in which more than 90% of cases carry oncogenic $KRAS$ mutations (Figure S4D) (Biankin et al., 2012). Lastly, we observed strong pCDC25B staining in xenograft tumors derived from H460 [$KRAS^{mut}$] and H1437 [$CDKN2A^{del}$] synergistic cell lines, in contrast to tumors derived from non-synergistic cells (Figure S4D).

To address the functional impact of combined Chk1- and MK2 inhibition on synergistic and non-synergistic cells, we next exposed the cell line panel shown in Figure 2E to PF477736 (0.5 μM), PF3644022 (2.0 μM), or a combination regimen for 12 hr. Although neither Chk1- nor MK2 inhibition alone led to a detectable repression of CDC25B phosphorylation, combination treatment completely abolished pCDC25B in the synergistic lines.

Coinciding with the complete removal of the inhibitory phosphorylation on CDC25B under combined Chk1/MK2 inhibition, we observed a marked increase in genotoxic stress in these cells, evidenced by strong γ-H2AX positivity (Figure 2E). In contrast, dual checkpoint inhibition did not result in the occurrence of detectable γ-H2AX staining in non-synergistic cell lines, whereas etoposide led to substantial genotoxic stress in these cells, evidenced by γ-H2AX staining and CDC25B phosphorylation (Figure 2E).

Our data prompted us to hypothesize that oncogene-driven replicative stress in the synergistic cell lines might lead to the constant induction of genotoxic damage, which is counteracted by tonic activity of Chk1 and MK2. Concordant with this hypothesis, we found that acute $KRAS^{G12D}$ expression led to the induction of genotoxic stress, evidenced by the occurrence of γ-H2AX foci and activation of Chk1 and MK2 in U2OS cells and MEFs (Figures S4E and S4F). Our data support a model in which oncogene-induced intrinsic hyperactivation of the checkpoint machinery is the common denominator of synergistic cell lines.

Checkpoint Abrogation Induces Mitotic Catastrophe in $KRAS$-Mutant Cancer Cells

A hallmark of mitotic catastrophe is mitotic entry in the presence of damaged DNA, resulting in the induction of apoptosis (Castedo et al., 2004). We showed that combined Chk1/MK2 inhibition prevented CDC25B phosphorylation, caused DNA damage, and selectively induced apoptosis in synergistic cell lines. We thus hypothesized that mitotic catastrophe might be the underlying mechanism leading to cell death of synergistic lines in response to combined Chk1/MK2 inhibition. To substantiate this hypothesis, we examined the distribution of genotoxic lesions, caused by combined Chk1/MK2 inhibition, across different cell cycle phases. We treated a panel of 6 synergistic and 4 non-synergistic cell lines with PF477736 (0.5 μM), PF3644022 (2.0 μM), or a combination for 0, 12, 24, or 48 hr (Figures 3A–3C, S4G, and S4H).

Checkpoint abrogation in the synergistic lines HCC44 and H1437 led to the accumulation of mitotic cells carrying DNA lesions, as evidenced by the appearance of a substantial γ-H2AX/pHH3 double-positive population after 24 hr (Figures 3A and 3B). In contrast, the same treatment did not induce γ-H2AX-positive mitotic cells in non-synergistic H2172 cells (Figure 3C). This difference in drug response between synergistic and non-synergistic cell lines was statistically significant (p < 0.005 for S and M phase) when the entire panel of 10 cell lines was analyzed (Figures S4G and S4H).

To prove that synergistic cell lines exposed to dual Chk1/MK2 blockade indeed undergo mitotic catastrophe, we stained synergistic and non-synergistic lines with antibodies against pHH3, γ-H2AX, and cleaved caspase-3 (CC3), a marker for apoptosis (Figures 3D–3I and S4I–S4K). Triple-positive cells were scored as undergoing mitotic catastrophe. Combination treatment induced mitotic catastrophe in the synergistic cell lines, as well as the Chk1 inhibitor-sensitive H1703 cells (Figures 3D–3I and S4I–S4K). These cells appeared to be committed to death specifically in mitosis, as no CC3 staining was observed in γ-H2AX-positive cells that did not also stain positive for pHH3 (Figures 3D and 3E, arrows versus arrowheads, Figures S4I–S4K). In contrast, non-synergistic H2172 and H1975 cells displayed no signs of mitotic catastrophe, even when treated with the combination therapy (Figures 3F, 3I, and S4I–S4K). Together, our data suggest that the apoptosis, which we observed in synergistic cells, results from mitotic catastrophe.

Combined Chk1/MK2 Inhibition Is an Effective Regimen for the Treatment of $KRAS$-Driven Xenograft Tumors

We next engrafted $NMRI^{nu/nu}$ mice with 11 synergistic and 2 non-synergistic control lines (Figures 4 and S5). Upon tumor formation, mice were treated with vehicle, PF477736 (15 mg/kg once daily [q.d.]), PF3644022 (10 mg/kg q.d.), or a combination for 14 days. Inhibition of Chk1 or MK2 alone did not substantially inhibit proliferation of the xenograft tumors (Figures 4A–4I and S5A–S5D). In contrast, combined Chk1/MK2 inhibition led to a significant reduction of the proliferation rates of tumors formed by $KRAS$- (p = 3.59×10^{-9}, n = 136, Figure 4J) or $BRAF$-mutant (p = 1.58×10^{-7}, n = 95, Figure 4K) cells, whereas control tumors grew under dual checkpoint abrogation (Figures 4H and 4I). We stained tumor sections for Ki67 (Figure S5E) and CC3 (Figure S5F) to gauge proliferation and apoptosis, respectively. Combined Chk1/MK2 inhibition resulted in a substantial reduction of Ki67 staining (Figure S5E) and a robust increase in CC3 positivity (Figure S5F) in tumors formed by $KRAS$-, $BRAF$-, or $CDKN2A$-altered cell lines. The combination regimen did not lead to any detectable changes in Ki67- or CC3 staining in control tumors (Figures S5E and S5F). No substantial changes in Ki67 and CC3 levels were observed in any tumor treated with single-agent PF3644022 or PF477736 (Figures S5E and S5F). These data suggest that the checkpoint addiction of $KRAS$- and $BRAF$-mutant, as well as $CDKN2A$-deleted cell lines, is preserved in vivo.

Autochthonous $Kras$- or $Braf$-Driven Tumors Display Checkpoint Addiction

We next analyzed the mutation spectrum of 995 cancer cell lines (Barretina et al., 2012). This analysis revealed that activating
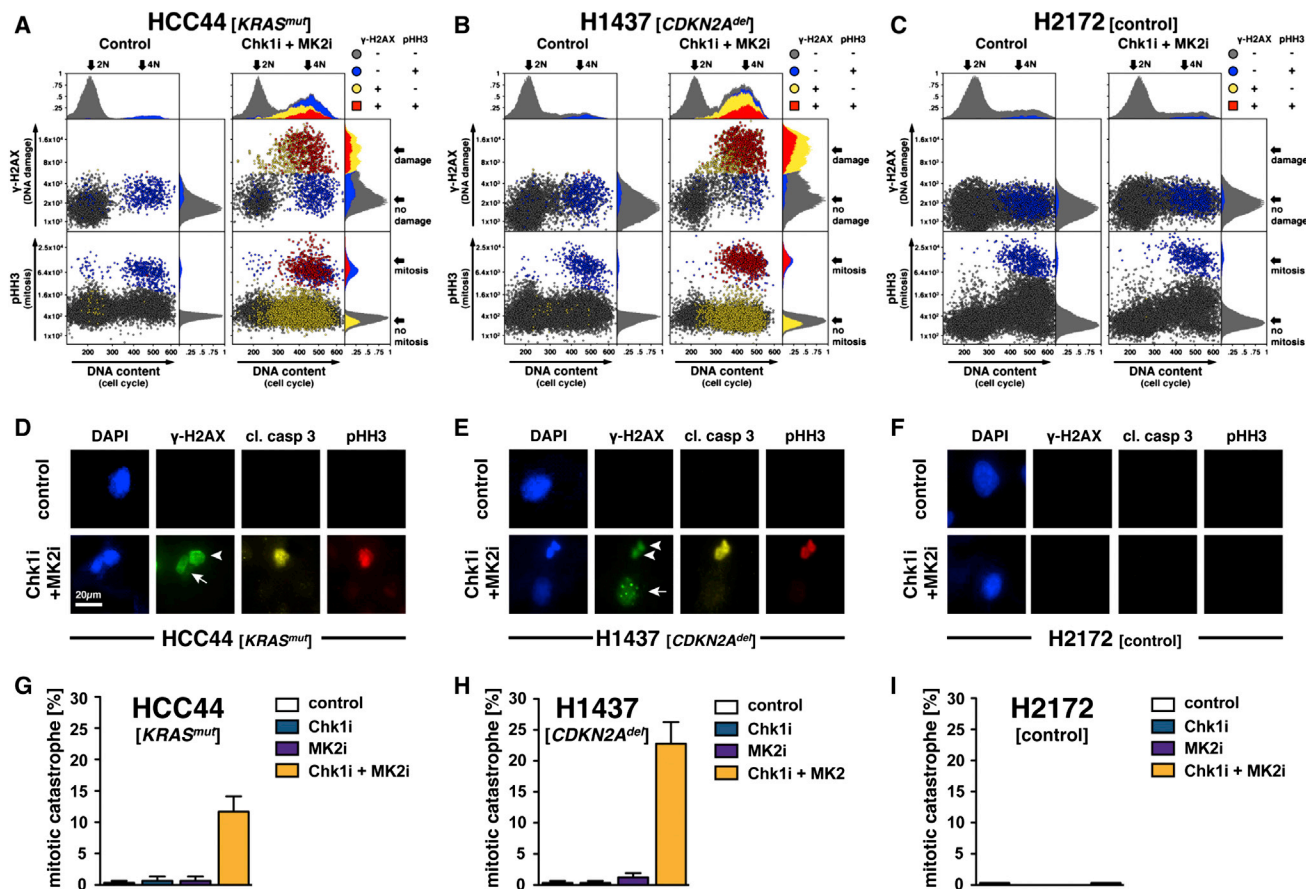
Figure 3. Checkpoint Abrogation Induces Mitotic Catastrophe in Synergistic Cell Lines

(A–C) Simultaneous Chk1/MK2 inhibition allows mitotic entry of cells under genotoxic stress. *KRAS*-mutant HCC44 (A), *CDKN2A*-deleted H1437 (B), and non-synergistic H2172 (C) cells were left untreated (control) or exposed to a combination of PF477736 (0.5 μM) and PF3644022 (2 μM) (Chk1i+MK2i) for 24 hr. Cells were stained for pHH3 and γ-H2AX and analyzed using flow cytometry. Cellular DNA content (PI staining) is plotted against γ-H2AX- (top) and pHH3 signals (bottom). Cells that were γ-H2AX and pHH3 positive are shown as red squares. Cells that were exclusively positive for either γ-H2AX or pHH3 are colored in blue or yellow, respectively. Double-negative cells are shown in gray. See Figures S4G and S4H for a statistical analysis of these experiments.

(D–F) Combined Chk1/MK2 inhibition selectively induces apoptosis in mitotic cells. HCC44 (D), H1437 (E), and H2172 (F) cells were either left untreated (control) or exposed to PF477736 (0.5 μM, Chk1i), PF3644022 (2 μM, MK2i), or a combination regimen (Chk1i+MK2i) for 24 hr. Cells were stained for γ-H2AX, pHH3, and CC3. Representative staining immunofluorescence (IF) images are shown. Arrowheads point to triple-positive cells, which undergo mitotic catastrophe. Arrows mark DNA-damaged γ-H2AX-positive cells, which are not in mitosis (pHH3 negative) and do not display signs of apoptotic cell death (CC3 negative).

(G–I) Quantification of the IF experiments shown in (D–F). Bar graphs display the average fraction of triple-positive cells (mitotic catastrophe, y axis) when left untreated (control) or after exposure to PF477736 (0.5 μM, Chk1i), PF3644022 (2 μM, MK2i), or a combination regimen (Chk1i+MK2i) for 24 hr. For each condition, 250–500 independent cells were counted. Error bars display SDs. See Figures S4I–S4K for IF experiments on three additional cell lines.

mutations in *KRAS* or *BRAF* (p = 0.0004), as well as *CCND1* amplifications (p = 0.008), appear to be mutually exclusive lesions, suggesting that a single alteration within the KRAS-BRAF-MEK-ERK-Cyclin D1 pathway is sufficient for its tonic activation (Figure S6A). Similarly, co-occurrence of alterations in *TP53*, *CDKN2A*, and *MDM2* was also significantly underrepresented (p = 0.001 and p = 0.01, respectively) (Figure S6A). Furthermore, cell lines carrying alterations in *KRAS*, *BRAF*, or *CCND1* (*KRAS* cluster) were significantly (p = 0.01) enriched for co-occurring alterations in *TP53*, *CDKN2A*, or *MDM2* (*TP53* cluster) (Figure S6A). These data may suggest that cell lines carrying alterations in the *KRAS* cluster might adapt to oncogenic stress by simultaneous inactivation of the *TP53* cluster.

We next correlated genomic data with survival of lung adenocarcinoma patients (Cancer Genome Atlas Research Network, 2014) (Figure S6B). This analysis revealed that patients with alterations in both the *KRAS*- and *TP53* clusters displayed significantly (p = 6 × 10^{-4}) reduced overall survival, compared to patients with mutations in the *KRAS*- but not the *TP53* cluster (Figure S6B). We next aimed to assess the efficacy of dual-checkpoint inhibition in a mouse model that genetically mimics these high-risk tumors carrying mutations in the *KRAS*- and *TP53* clusters. For this purpose, we employed an established mouse model that allows conditional expression of *Kras^G12D* and simultaneous *Tp53* deletion (DuPage et al., 2009) (Figure 5A). Coherent with the clinical scenario (Figure S6B),
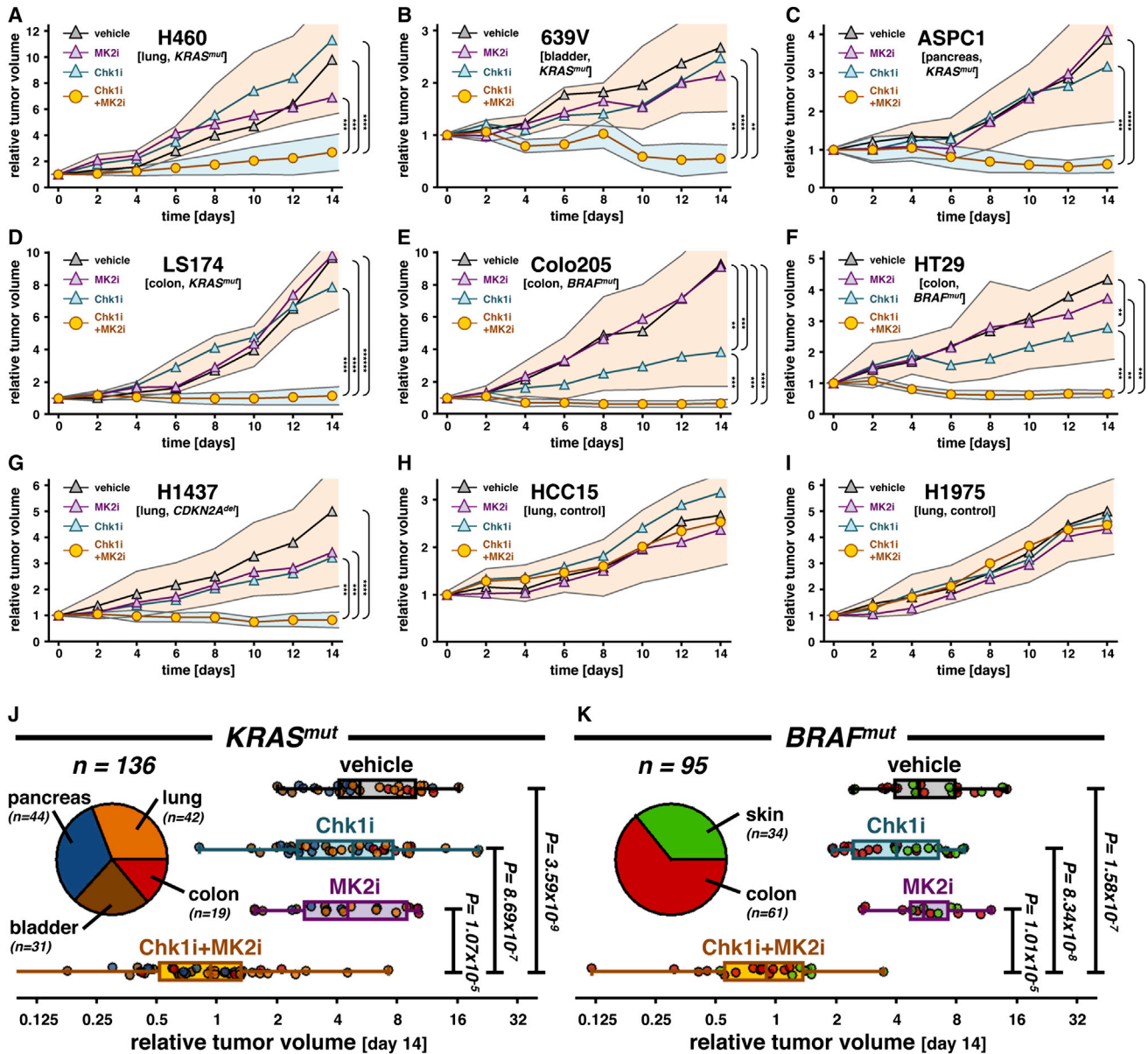
Figure 4. Xenograft Tumors Derived from Synergistic Cell Lines Are Sensitive to Combined Chk1/MK2 Inhibition

(A–I) Simultaneous Chk1/MK2 inhibition inhibits growth of xenograft tumors formed by synergistic cell lines. Mice were engrafted with *KRAS*-mutant H460 (A), 639V (B), ASPC1 (C), and LS174 cells (D), as well as *BRAF*-mutant Colo205 (E), HT29 cells (F), and *CDKN2A*-deleted H1437 cells (G) and non-synergistic HCC15 (H) or H1975 (I) controls. Upon tumor formation, mice were treated with vehicle, PF3644022 (10 mg/kg, q.d., MK2i), PF477736 (15 mg/kg, q.d., Chk1i), or a combination of both compounds (Chk1i+MK2i) for 14 days. Curves display average values of three independent experiments per group. Envelopes encode SD of the combination treatment group (turquoise) or combined SD of control, Chk1-, and MK2 inhibitor-treated groups (orange). Significant differences are marked by asterisks. See Figures S5A–S5D for four additional cell lines. See Figures S5E and S5F for an immunohistochemical analysis of these tumors after therapy completion.

(J and K). Therapeutic response across 136 *KRAS*- (J) and 95 *BRAF*-mutant (K) xenograft tumors. Box-and-whiskers plots display relative tumor volumes (x axis) of *KRAS*- (J) and *BRAF*-mutant (K) tumors after 14 day exposure to vehicle, Chk1 inhibitor, MK2 inhibitor, or a combination regimen. Boxes mark the interquartile range, transverse lines represent the median, and whiskers range from minimal to maximal value. Each circle represents the relative volume of an individual tumor on day 14. Circle colors encode tumor histology. Groups were compared by two-tailed Student's t test. Inset: pie chart representation of histotypes in the xenograft tumor panel.

Kras^{LSL-G12D/+};*Tp53^{flox/flox}* (KP) animals display a significantly (p = 4 × 10^{−3}) worse survival compared to *Kras^{LSL-G12D/+}*; *Tp53^{wt/wt}* animals (Figure S6C).

We next validated dual-checkpoint inhibition as a therapeutic approach in *KP* mice. Upon tumor formation (Figure 5B), we administered a 7 day course of PF477736 (15 mg/kg q.d.) and
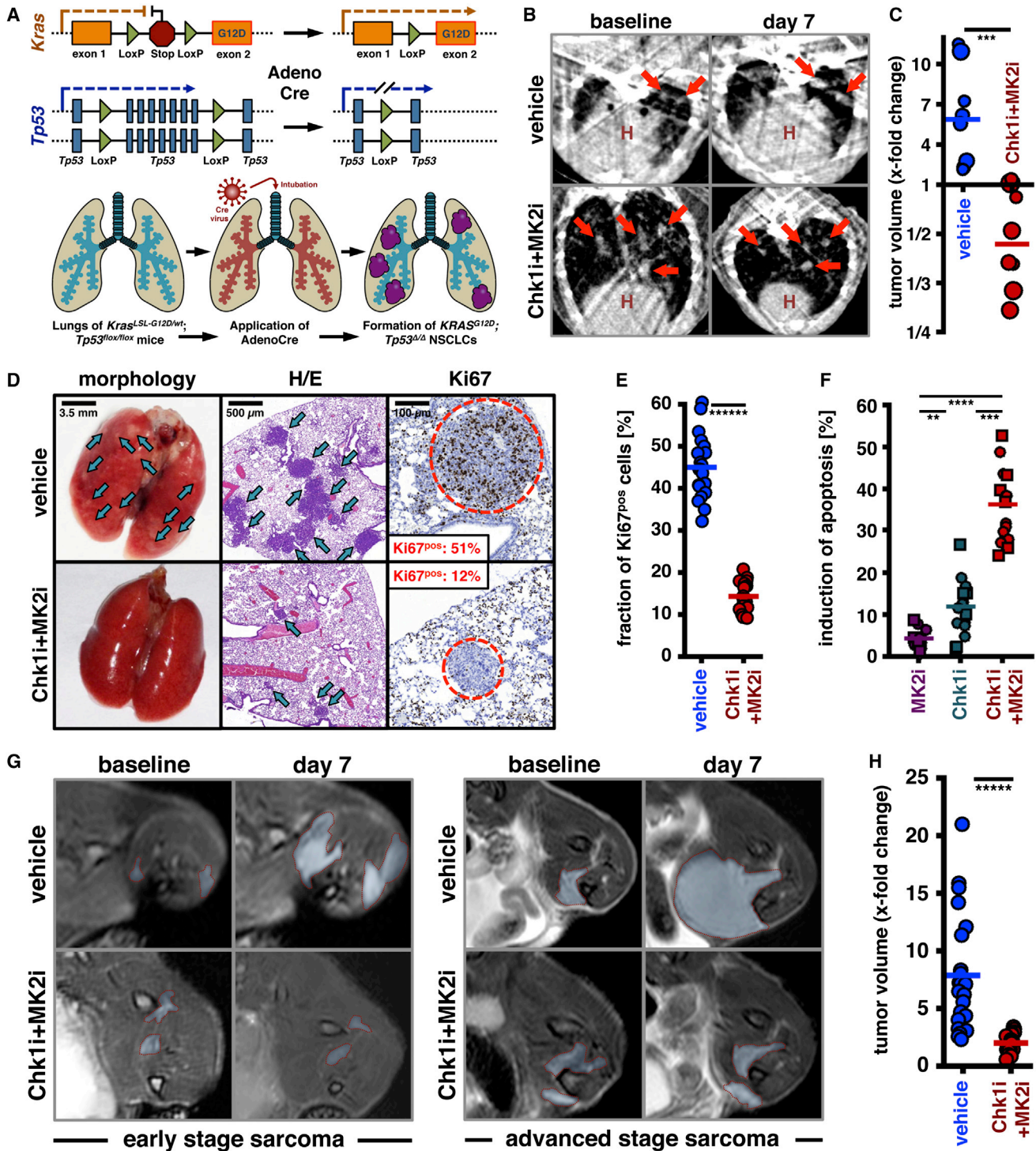
Figure 5. Response of an Autochthonous *Kras*-Driven Lung Adenocarcinoma Model to Checkpoint-Abrogating Therapy

(A) Schematic representation of the mouse model. See Figures S6A–S6C for a detailed comparison of this mouse model with clinical data.

(B and C) μCT-based response assessment of tumor nodules. 5 weeks after AdCre application, lungs were imaged (μCT) to confirm tumor formation (baseline image). After 7 days of vehicle (top) or checkpoint-abrogating therapy (bottom), mice were re-imaged. (B) μCT images before (left) and after completion of treatment (right) are shown. Red arrows point to nodular target lesions used for response evaluation (RECIST 1.1). The heart is indicated (H). (C) Lesion volumes were quantified after treatment and normalized to the pre-treatment values (x-fold change, y axis). Volume changes in the therapy cohort (red) were compared with the vehicle-treated control group (blue) by two-tailed Student's t test. Circle sizes encode the initial lesion volume. Significance level is indicated by asterisks.

(legend continued on next page)

PF3644022 (10 mg/kg q.d.). Response was evaluated by micro computed tomography (μCT). This analysis revealed significant (p = 0.004) differences between the groups. Whereas vehicle-treated tumors showed a volume gain within the 7 day observation period, lesion shrinkage was observed in most animals treated with the combination therapy (Figures 5B and 5C). This CT-morphological tumor response is reflected by an obvious reduction in relative tumor content and a significant (p = 1.3 × 10^{-15}) reduction in Ki67-positive tumor cells in treated animals (Figures 5D and 5E).

To address whether sensitivity to checkpoint abrogation is preserved in individual tumor clones, we isolated cells from 15 KP tumors. Combined Chk1/MK2 inhibition induced apoptosis in all 15 clones, whereas isolated MK2- or Chk1 inhibition failed to induce substantial levels of apoptosis in these primary cells (Figure 5F). We note that 6 of the 15 lung cancer cell lines were isolated from animals that succumbed to tumors that relapsed after an initial cisplatin treatment (Figure 5F, squares), suggesting that combined Chk1/MK2 inhibition might be a therapeutic option for cisplatin-resistant lung cancer patients.

Next, we asked whether combined Chk1/MK2 inhibition increases the survival of KP animals. We administered three 5 day cycles of PF477736 (15 mg/kg q.d.) and PF3644022 (10 mg/kg q.d.) or vehicle control 5 weeks after AdCre inhalation. As a control, we treated a separate cohort of animals with cisplatin (7.5 mg/kg, 1× per week, for three cycles). Median survival of vehicle-treated animals was 115 days, and cisplatin treatment failed to significantly (p = 0.956) enhance this survival (117 days). In contrast, dual checkpoint abrogation significantly prolonged median survival (150 days), compared with vehicle (p = 0.027) and cisplatin (p = 0.007) controls (Figure S6D).

To ask whether checkpoint addiction was preserved in an independent KRAS-driven entity, we employed a model of high-grade sarcoma (Kirsch et al., 2007). Upon sarcoma formation, animals received a 7 day course of PF477736 (15 mg/kg q.d.) and PF3644022 (10 mg/kg q.d.) or vehicle. Response was monitored by MRI imaging and revealed a significant (p = 2.38 × 10^{-5}) difference in tumor volume change between animals receiving vehicle or checkpoint abrogation (Figures 5G and 5H). Whereas control animals showed significant tumor progression (p = 0.0016), no significant volume change was observed under treatment with combined Chk1/MK2 inhibition (p = 0.193).

Finally, we assessed the effect of dual-checkpoint abrogation in a Braf-driven mouse model. We employed Vil-Cre; Braf$^{LSL-V637E/+}$;p16$^{Ink4a*/+}$ mice, which develop intestinal carcinomas through a hyperplasia/adenoma/carcinoma sequence (Rad et al., 2013). At the age of 12 months, mice were treated with a combination of PF477736 (15 mg/kg q.d.) and PF3644022 (10 mg/kg q.d.) for 7 days. Tumor response was assessed through IHC-based detection of CC3. This analysis revealed a significant (p = 0.017) increase of CC3 positivity scores compared with baseline staining intensities of untreated tumors (Figures S6E and S6F). In particular, CC3 was detectable at medium or high levels in 92% (11/12) of all treated tumors (scores 2, 3). In marked contrast, 93% (13/14) of the control tumors were CC3 negative or displayed only low CC3 positivity (scores 1, 2) (Figures S6E and S6F). Thus, dual checkpoint abrogation induced apoptosis in most Braf-driven individual intestinal lesions.

Clinical Extrapolation of Combined Chk1/MK2 Inhibition in *KRAS*-Mutant Adenocarcinomas

To ask whether the intrinsic checkpoint activation that we observed in KRAS-driven cancer cells is preserved in human tumors, we compiled a cohort of 20 lung and 40 colon adenocarcinoma samples with known KRAS status. We performed an IHC-based assessment of pChk2 and pMK2 levels, in order to profile basal checkpoint activation. IHC intensity scores of pChk2 were significantly higher in KRAS-mutant lung (p = 0.022) and colon carcinomas (p = 0.0034), compared with non-mutant controls (Figures 6A and 6B). We further found that staining intensities of pMK2 paralleled the pChk2 intensity scores (Figures 6A and 6B). These data suggest that KRAS-driven tumors display intrinsically activated cell-cycle checkpoints, rationalizing their Chk1/MK2 dependence.

We next assessed the effects of combined Chk1/MK2 inhibition in clinical specimens isolated from lung adenocarcinoma patients. Cells were isolated from pleural effusions of 14 patients who had received prior chemotherapy. Samples were characterized by high-coverage sequencing of 102 exons in 13 genes (Figure S7A). Upon isolation, cells were immediately treated with PF477736 (0.5 μM), PF3644022 (2.0 μM), or a combination

(D) Checkpoint-abrogating therapy represses tumor cell proliferation. Chk1/MK2 inhibition led to tumor volume reduction (middle) and a significant reduction in Ki67 scores (right), indicating reduced proliferation. Turquoise arrows point to nodular tumor lesions (left middle). Red circles mark exemplary nodular lesions, for which Ki67 proliferation scores are annotated (right). Scale bars, 3.5 mm (left), 500 μm (middle), and 100 μm (right).
(E) Quantification of Ki67 scores of individual nodular lesions treated with vehicle control or combined Chk1/MK2 inhibition. Significance was calculated by two-tailed Student's t test. Significance is indicated by asterisks.
(F) Cell lines (n = 15) were derived from individual tumors and exposed to PF3644022 (2 μM, MK2i), PF477736 (0.5 μM, Chk1i), or a combination (Chk1i+MK2i) for 72 hr. Apoptosis was assessed by flow-cytometry-based measurement of the Annexin V/PI double-positive population and compared by two-tailed Student's t test. Squares mark cell lines from mice that developed cisplatin resistance, whereas circles encode lesions from chemotherapy-naive mice. Significance level is indicated by asterisks.
(G and H) MRI-based response evaluation of high-grade sarcomas. 30 days after AdCre injection, hind legs were imaged using a small-animal solenoid MRI coil (baseline image). After completion of a 7 day treatment regimen with vehicle (top) or combined Chk1/MK2 inhibition (bottom), mice were re-imaged. (G) Images of early-stage (left) and late-stage (right) sarcomas before (left) and after therapy (right) are shown in a spectral fat suppression MRI sequence. Blue areas highlight sarcoma expansion. (H) Sarcoma volume ratios before and after treatment (x-fold change, y axis) are compared between vehicle and therapy cohorts by two-tailed Student's t test. Significance level is indicated by asterisks.
See Figure S6D for survival of the Kras-driven lung cancer model under combination therapy. See Figures S6E and S6F for response of an autochthonous Braf-driven colon cancer model to combined Chk1/MK2 inhibition.
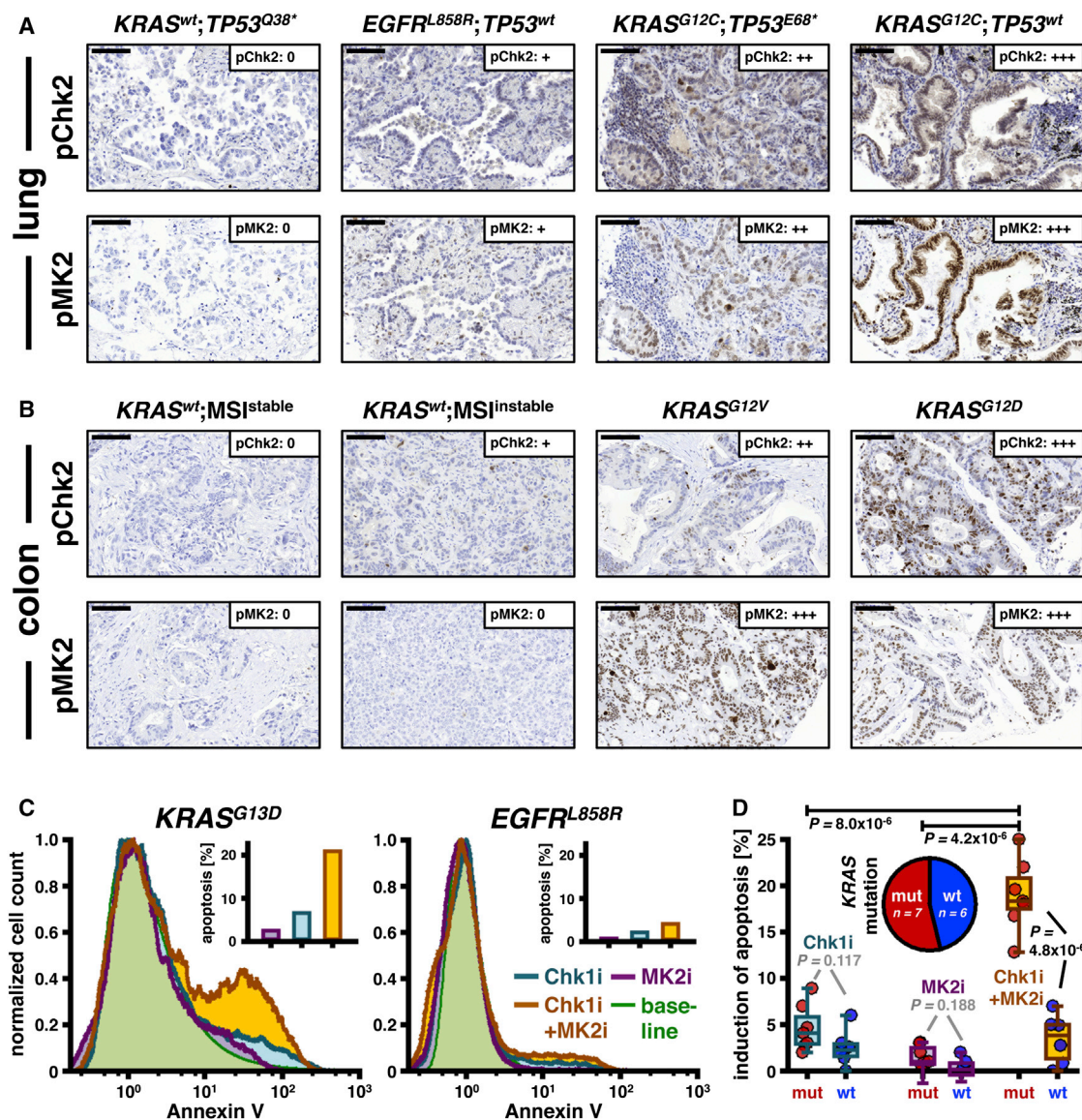
Figure 6. Clinical Extrapolation of a Synergistic Interaction between Chk1- and MK2 Inhibitors

(A and B) A cohort of 20 lung (A) and 40 colon (B) adenocarcinoma patient biopsies was stained for pChk2 and pMK2 to assess intrinsic checkpoints activation. Median staining intensities of tumor cells were scored on a 4-tier scale. Exemplary images are shown for each staining intensity score together with genomic annotation in *KRAS*, *EGFR*, and *TP53*, as well as microsatellite instability (MSI). Scale bars, 100 μm.

(C and D) Malignant cells from 13 pleural effusions were cultivated and either left untreated (green, baseline) or exposed to PF477736 (0.5 μM, Chk1i), PF3644022 (2 μM, MK2i), or a combination regimen (Chk1i+MK2i) for 48 hr. Apoptosis was quantified by flow cytometry. Inset: total apoptosis levels of each therapy regimen, quantified as the area under the Annexin V histogram. (C) Apoptosis levels were compared between *KRAS*-mutant and non-mutant samples by two-tailed Student's t test. Significance values are denoted for each therapeutic intervention. (D) inset: pie chart representation of the *KRAS* mutation status in the lung cancer patient cohort. See Figure S7A for a detailed genomic characterization of the patient cohort. See Figure S7B for a similar examination of cells isolated from a *BRAF*-mutant patient. See Figures S7C and S7D for synergistic effects of Chk1- and MK2 inhibitors in primary pancreatic adenocarcinoma cells.

for 48 hr (Figures 6C and 6D). Upon completion of drug exposure, apoptosis measurements revealed that *KRAS*-mutant tumor cells (n = 7) were significantly (p = 4.8 × 10^{-6}) more sensitive to the combination treatment than cells lacking *KRAS* or *BRAF* mutations (n = 6) (Figures 6C and 6D). Furthermore, combined Chk1/MK2 inhibition induced massive apoptosis in primary tumor cells isolated from a pleural effusion of a patient with

BRAF^{N581S}-mutant (*KRAS*^{wt}) lung adenocarcinoma (Figure S7B). Single-agent Chk1- and MK2 inhibitors did not have significant apoptotic effects on patient-derived primary cells (p = 0.117 and p = 0.188, respectively) (Figures 6C, 6D, and S7B).

To validate these results, we employed *KRAS*-mutant pancreatic adenocarcinoma cells isolated from five independent human tumor specimens (Vermeulen et al., 2008). Isolated Chk1 or MK2
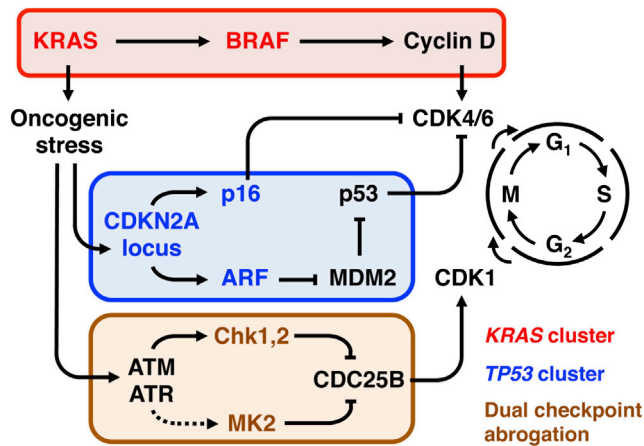
Figure 7. A Simplified Model for an Actionable Synergistic Interaction between Chk1- and MK2 Inhibitors in *KRAS*-Mutant Adenocarcinomas

Oncogenic stress induced by *KRAS* mutations (*KRAS* cluster) leads to the induction of DNA damage. Loss of functional p53 signaling either through deletion of *CDKN2A*, amplification of *MDM2*, or *TP53* alterations (*TP53* cluster) prevents DNA damage-induced apoptosis. In parallel, loss of functional p53 leads to destabilized cell-cycle regulation (e.g., through loss of p21 induction) and thus induces checkpoint kinase dependence. Hence, simultaneous Chk1/MK2 inhibition leads to a complete checkpoint collapse and subsequent demise of *KRAS*-mutant cells in mitotic catastrophe.

inhibition did not result in any cytotoxicity, whereas combined checkpoint abrogation led to massive apoptosis (Figures S7C and S7D, p = 7.16 × 10^{-7}) in these cells. Thus, our data recommend dual-checkpoint blockade as a therapeutic means to treat *KRAS*-driven human malignancies.

DISCUSSION

Oncogenic Mutations in *KRAS* Are Associated with Cell-Cycle Checkpoint Addiction

We showed that oncogenic *KRAS* mutations are associated with addiction to Chk1-/MK2-mediated checkpoints. We demonstrated that acute expression of oncogenic *KRAS* induces genotoxic damage. Intriguingly, we showed that *KRAS*-driven cell lines are enriched for checkpoint-destabilizing cooperating lesions, such as *CDKN2A* deletions or *TP53* mutations. These data indicate that malignant transformation of *KRAS*-driven neoplastic lesions requires the concomitant inactivation of components of the cell-cycle-regulating *CDKN2A*- or *TP53* network (Figure 7). Coherent with this hypothesis, early premalignant lesions were recently shown to frequently display an accumulation of DNA damage. This genotoxic damage in pre-malignant lesions leads to the activation of the DDR network. As tumorigenesis progresses, incipient tumor cells appear to inactivate certain components of the DDR (e.g., ATM, Chk2, and p53) to overcome oncogene-induced senescence, suggesting that silencing DDR signaling is a prerequisite for transformation (Bartkova et al., 2006). This destabilization of the cell-cycle checkpoint machinery, on the background of genotoxic stress-inducing KRAS signaling, might rationalize the addiction of *KRAS*-driven tumor

cells to the remaining checkpoint kinases. Chk1 and MK2, which have both been shown to be critical components of the G$_2$/M checkpoint, might be essential for preventing mitotic entry of cells suffering from genotoxic damage (Reinhardt and Yaffe, 2013). In line with this hypothesis, we found CDC25B, a common substrate of these kinases, to be constitutively phosphorylated in *KRAS*-mutant carcinomas, suggesting that pCDC25B might be a suitable biomarker to predict cell-cycle checkpoint addiction. Furthermore, we could show that simultaneous inhibition of these checkpoint kinases in *KRAS*-driven cancer cells leads to the accumulation of mitotic cells carrying genotoxic lesions. We found that these damaged cells in M phase undergo mitotic catastrophe, mechanistically rationalizing the synergistic interaction observed between Chk1- and MK2 inhibitors. Thus, our data now provide a strong rationale for the clinical validation of combined checkpoint abrogation through the use of Chk1- and MK2 inhibitors in patients carrying *KRAS*-driven malignancies.

EXPERIMENTAL PROCEDURES

High-Throughput Viability Measurements

Cells were seeded into sterile 96-well plates and treated with various concentration pairs of two different compounds for 96 hr. After completion of drug exposure, we determined the relative ATP content in each well and normalized it to a vehicle-treated control. We examined these measurements for synergistic effects between both compounds using the PreCISE software (Data S1).

Autochthonous Murine Cancer Models

We used *LSL-Kras$^{G12D/+}$;Tp53$^{flox/flox}$* (KP) mice as an autochthonous model for *KRAS*-mutant adenocarcinomas. In order to generate *Kras*-driven lung tumors, we applied a replication-deficient adenovirus expressing Cre to the lungs of 8-week-old KP mice in anesthesia. 5 weeks after virus inhalation, lungs were imaged by µCT imaging in order to confirm tumor formation. In order to induce *Kras*-driven high-grade soft tissue sarcomas, we applied Cre adenovirus to the hind legs of 6-week-old KP mice by intramuscular injection. 30 days after injection, hind legs were scanned by MR imaging in order to confirm sarcoma formation. We used *Vil-Cre; Braf$^{LSL-V637E/+}$;p16$^{Ink4a+/+}$* as an autochthonous model for *BRAF*-mutant colon cancer. These mice develop *Braf*-driven colorectal carcinomas at the age of 12 months. After tumor formation, animals were treated either with vehicle solution or with a combination therapy of PF3644022 (10 mg/kg) and PF477736 (15 mg/kg) by daily intraperitoneal injections. After completion of the combination therapy, we examined the tumor response either by µCT- or MR-based re-imaging or by staining tumors for cleaved caspase-3.

Further details about the mathematical analysis, cell culture methods and viability screening, crystal structure analysis, flow cytometry, clonogenic survival assays, retro- and lentivirus production, immunoblotting, immunofluorescence, murine cancer models, µCT and MRI imaging, immunohistochemistry, passaging, cultivation, and parallel sequencing of patient material are described in the Supplemental Experimental Procedures.

SUPPLEMENTAL INFORMATION

Supplemental Information includes Supplemental Experimental Procedures, seven figures, one table, and two data files and can be found with this article online at http://dx.doi.org/10.1016/j.cell.2015.05.053.

REFERENCES

Barretina, J., Caponigro, G., Stransky, N., Venkatesan, K., Margolin, A.A., Kim, S., Wilson, C.J., Lehár, J., Kryukov, G.V., Sonkin, D., et al. (2012). The Cancer Cell Line Encyclopedia enables predictive modelling of anticancer drug sensitivity. Nature *483*, 603–607.

Bartkova, J., Rezaei, N., Liontos, M., Karakaidos, P., Kletsas, D., Issaeva, N., Vassiliou, L.V., Kolettas, E., Niforou, K., Zoumpourlis, V.C., et al. (2006). Oncogene-induced senescence is part of the tumorigenesis barrier imposed by DNA damage checkpoints. Nature *444*, 633–637.

Biankin, A.V., Waddell, N., Kassahn, K.S., Gingras, M.C., Muthuswamy, L.B., Johns, A.L., Miller, D.K., Wilson, P.J., Patch, A.M., Wu, J., et al.; Australian Pancreatic Cancer Genome Initiative (2012). Pancreatic cancer genomes reveal aberrations in axon guidance pathway genes. Nature *491*, 399–405.

Cancer Genome Atlas Research Network (2014). Comprehensive molecular profiling of lung adenocarcinoma. Nature *511*, 543–550.

Castedo, M., Perfettini, J.L., Roumier, T., Andreau, K., Medema, R., and Kroemer, G. (2004). Cell death by mitotic catastrophe: a molecular definition. Oncogene *23*, 2825–2837.

Curtin, N.J. (2012). DNA repair dysregulation from cancer driver to therapeutic target. Nat. Rev. Cancer *12*, 801–817.

Dietlein, F., Thelen, L., Jokic, M., Jachimowicz, R.D., Ivan, L., Knittel, G., Leeser, U., van Oers, J., Edelmann, W., Heukamp, L.C., and Reinhardt, H.C. (2014). A functional cancer genomics screen identifies a druggable synthetic lethal interaction between MSH3 and PRKDC. Cancer Discov. *4*, 592–605.

DuPage, M., Dooley, A.L., and Jacks, T. (2009). Conditional mouse lung cancer models using adenoviral or lentiviral delivery of Cre recombinase. Nat. Protoc. *4*, 1064–1072.

Jackson, S.P., and Bartek, J. (2009). The DNA-damage response in human biology and disease. Nature *461*, 1071–1078.

Kirsch, D.G., Dinulescu, D.M., Miller, J.B., Grimm, J., Santiago, P.M., Young, N.P., Nielsen, G.P., Quade, B.J., Chaber, C.J., Schultz, C.P., et al. (2007). A spatially and temporally restricted mouse model of soft tissue sarcoma. Nat. Med. *13*, 992–997.

Lehár, J., Krueger, A.S., Avery, W., Heilbut, A.M., Johansen, L.M., Price, E.R., Rickles, R.J., Short, G.F., 3rd, Staunton, J.E., Jin, X., et al. (2009). Synergistic drug combinations tend to improve therapeutically relevant selectivity. Nat. Biotechnol. *27*, 659–666.

Loewe, S. (1953). The problem of synergism and antagonism of combined drugs. Arzneimittelforschung *3*, 285–290.

Rad, R., Cadiñanos, J., Rad, L., Varela, I., Strong, A., Kriegl, L., Constantino-Casas, F., Eser, S., Hieber, M., Seidler, B., et al. (2013). A genetic progression model of Braf(V600E)-induced intestinal tumorigenesis reveals targets for therapeutic intervention. Cancer Cell *24*, 15–29.

Reinhardt, H.C., and Yaffe, M.B. (2013). Phospho-Ser/Thr-binding domains: navigating the cell cycle and DNA damage response. Nat. Rev. Mol. Cell Biol. *14*, 563–580.

Reinhardt, H.C., Hasskamp, P., Schmedding, I., Morandell, S., van Vugt, M.A.T.M., Wang, X., Linding, R., Ong, S.-E., Weaver, D., Carr, S.A., and Yaffe, M.B. (2010). DNA damage activates a spatially distinct late cytoplasmic cell-cycle checkpoint network controlled by MK2-mediated RNA stabilization. Mol. Cell *40*, 34–49.

Vermeulen, L., Todaro, M., de Sousa Mello, F., Sprick, M.R., Kemper, K., Perez Alea, M., Richel, D.J., Stassi, G., and Medema, J.P. (2008). Single-cell cloning of colon cancer stem cells reveals a multi-lineage differentiation capacity. Proc. Natl. Acad. Sci. USA *105*, 13427–13432.